

The inverse Kalman filter

Xinyi Fang and Mengyang Gu*

Abstract

We introduce the inverse Kalman filter, which enables exact matrix-vector multiplication between a covariance matrix from a dynamic linear model and any real-valued vector with linear computational cost. We integrate the inverse Kalman filter with the conjugate gradient algorithm, which substantially accelerates the computation of matrix inversion for a general form of covariance matrix, where other approximation approaches may not be directly applicable. We demonstrate the scalability and efficiency of the proposed approach through applications in nonparametric estimation of particle interaction functions, using both simulations and cell trajectories from microscopy data.

1 Introduction

Dynamic linear models (DLMs) or linear state space models are ubiquitously used in modeling temporally correlated data [38, 5]. Each observation $y_t \in \mathbb{R}$ in DLMs is associated with a q -dimensional latent state vector $\boldsymbol{\theta}_t$, defined as:

$$y_t = \mathbf{F}_t \boldsymbol{\theta}_t + v_t, \quad v_t \sim \mathcal{N}(0, V_t), \quad (1)$$

$$\boldsymbol{\theta}_t = \mathbf{G}_t \boldsymbol{\theta}_{t-1} + \mathbf{w}_t, \quad \mathbf{w}_t \sim \mathcal{MN}(\mathbf{0}, \mathbf{W}_t), \quad (2)$$

where \mathbf{F}_t and \mathbf{G}_t are matrices of dimensions $1 \times q$ and $q \times q$, respectively, \mathbf{W}_t is a $q \times q$ covariance matrix for $t = 2, \dots, N$, and the initial state vector $\boldsymbol{\theta}_1 \sim \mathcal{MN}(\mathbf{b}_1, \mathbf{W}_1)$ with $\mathbf{b}_1 = \mathbf{0}$ assumed herein. The dependent structure of DLMs is illustrated in Fig. 1(a).

DLMs are a large class of models that include many widely used processes, such as autoregressive and moving average processes [27, 28]. Some Gaussian processes with commonly used covariance functions, including the Matérn covariance with a half-integer roughness parameter [13], can also be represented as DLMs [39, 14], with closed-form expressions for \mathbf{F}_t , \mathbf{G}_t and \mathbf{W}_t . This connection, summarized in the Supplementary Material, enables differentiable Gaussian processes to be used for scalably estimating smooth latent functions from noisy observations.

The Kalman filter (KF) provides a fast approach for estimating latent states and computing likelihood functions in DLMs, which scales linearly with the number of observations [17], as reviewed in Appendix A. In particular, the KF enables efficient computation of $\mathbf{L}^{-1}\mathbf{u}$ for any N -dimensional vector \mathbf{u} in $\mathcal{O}(q^3N)$ operations, where \mathbf{L} is the Cholesky factor of the covariance matrix $\boldsymbol{\Sigma} = \text{cov}[\mathbf{y}_{1:N}] = \mathbf{L}\mathbf{L}^T$, summarized in Lemma A2 in the Appendix.

Computational challenges remain for high-dimensional state space models and scenarios where the KF cannot be directly applied, such as the dependent structure shown in Fig. 1(b), where each observation y_i can be associated with multiple latent states. This interaction structure, introduced in Section 3, is common in physical models, including molecular dynamics simulation [29]. A

*The authors contribute equally. Correspondence should be addressed to Mengyang Gu (mengyang@pstat.ucsb.edu)

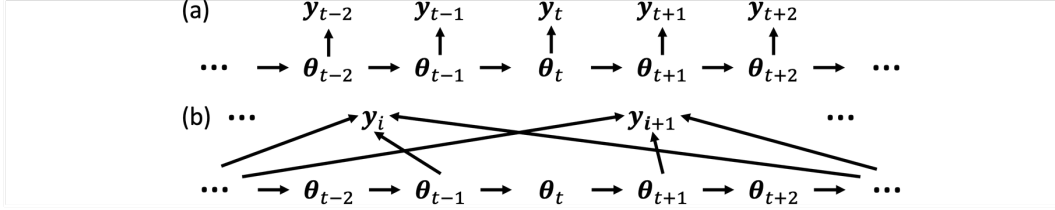


Figure 1: The dependent structure of the dynamic linear model (panel (a)) and particle dynamics (panel (b)).

way to overcome these challenges is to efficiently compute $\Sigma \mathbf{u}$ for any N -dimensional vector \mathbf{u} and utilize optimization methods such as conjugate gradient algorithms for computing predictive distributions [16]. This strategy has been used to approximate the maximum likelihood estimator of parameters in Gaussian processes [33, 26]. Yet, each conjugate gradient iteration requires matrix-vector multiplication, which involves $\mathcal{O}(N^2)$ operations and storage, making it prohibitive for large N .

To address this issue, we introduce the *inverse Kalman filter* (IKF), which computes $\mathbf{L} \mathbf{u}$ and $\mathbf{L}^T \mathbf{u}$ with $\mathcal{O}(q^3 N)$ operations without approximation, where \mathbf{L} is the Cholesky factor of any $N \times N$ DLM-induced covariance Σ and \mathbf{u} is an N -dimensional vector. The complexity is significantly smaller than $\mathcal{O}(N^2)$ in direct computation. The dimension of the latent states q does not exceed 3 in our applications, including commonly used models such as twice differentiable Gaussian processes with Matérn covariance in (15), often used as default in Gaussian process models.

The IKF algorithm can be extended to accelerate matrix multiplication and inversion, a key computational bottleneck in practice. We integrate the IKF into the conjugate gradient algorithm to scalably compute predictive distributions of observations with a general covariance structure:

$$\Sigma_y = \sum_{j=1}^J \mathbf{A}_j \Sigma_j \mathbf{A}_j^T + \Lambda, \quad (3)$$

where Σ_j is a DLM-induced covariance matrix, \mathbf{A}_j is sparse, and Λ is a diagonal matrix. This structure appears in nonparametric estimation of particle interactions, which will be introduced in Section 3. Both real and simulated studies involve numerous particles over a long time period, where conventional approximation methods [35, 20, 23, 3, 7, 10] are not applicable. This covariance structure also appears in other applications, including varying coefficient models [15] and estimating incomplete lattices of correlated data [32]. Though we focus on nonparametric estimation of particle interaction functions in this work, we also apply our approach to the latter in Section S5 and provide numerical comparisons with various approximation methods in Section S9 of the Supplementary Material.

2 Inverse Kalman filter

In this section, we introduce an exact algorithm for computing $\Sigma \mathbf{u}$ with $\mathcal{O}(q^3 N)$, where \mathbf{u} is an N -dimensional real-valued vector and $\Sigma = \text{cov}[\mathbf{y}_{1:N}]$ is an $N \times N$ covariance matrix of observations induced by a DLM with q latent states in Eqs. (1)-(2). This algorithm is applicable to any DLM specified in Eqs. (1)-(2). Denote $\Sigma = \mathbf{L} \mathbf{L}^T$, where the Cholesky factor \mathbf{L} does not need to be explicitly computed in our approach. We develop fast algorithms to compute $\tilde{\mathbf{x}} = \mathbf{L}^T \mathbf{u}$ and $\mathbf{x} = \mathbf{L} \tilde{\mathbf{x}}$ by Lemma 1 and Lemma 2, respectively, each with $\mathcal{O}(q^3 N)$ operations. Detailed proofs of these

Algorithm 1 Inverse Kalman filter (IKF) for computing $\Sigma \mathbf{u}$.

Input: $\mathbf{F}_t, \mathbf{G}_t, \mathbf{W}_t, t = 1, \dots, N$, an N -dimensional vector \mathbf{u} .

- 1: Use Kalman filter from Lemma A1 to compute \mathbf{B}_t, Q_t , and \mathbf{K}_t for $t = 1, \dots, N$.
- 2: Use Lemma 1 to compute $\tilde{\mathbf{x}} = \mathbf{L}^T \mathbf{u}$.
- 3: Use Lemma 2 to compute $\mathbf{x} = \mathbf{L} \tilde{\mathbf{x}}$.

Output: \mathbf{x} .

lemmas are available in the Supplementary Material. In the following, u_t, x_t, \tilde{x}_t denote the t th element of the vector of \mathbf{u}, \mathbf{x} , and $\tilde{\mathbf{x}}$, respectively, and $L_{t',t}$ denotes the (t', t) th element of \mathbf{L} for t and $t' = 1, 2, \dots, N$.

Lemma 1 (Compute $\tilde{\mathbf{x}} = \mathbf{L}^T \mathbf{u}$ with linear computational cost). *For any N -dimensional vector \mathbf{u} , let $\tilde{x}_N = Q_N^{1/2} u_N$, $\tilde{x}_{N-1} = Q_{N-1}^{1/2} (\ell_{N,N-1} u_N + u_{N-1})$, and $\mathbf{g}_{N-1} = \mathbf{F}_N \mathbf{G}_N u_N$. For $t = N-2, \dots, 1$, iteratively compute \tilde{x}_t by*

$$\tilde{x}_t = Q_t^{\frac{1}{2}} \left(\tilde{\ell}_{t+1,t} + \ell_{t+1,t} u_{t+1} + u_t \right), \quad (4)$$

$$\mathbf{g}_t = \mathbf{g}_{t+1} \mathbf{G}_{t+1} + \mathbf{F}_{t+1} \mathbf{G}_{t+1} u_{t+1}, \quad (5)$$

where $\ell_{t+1,t} = \mathbf{F}_{t+1} \mathbf{G}_{t+1} \mathbf{K}_t$, $\tilde{\ell}_{t+1,t} = \mathbf{g}_{t+1} \mathbf{G}_{t+1} \mathbf{K}_t$, and \mathbf{K}_t is the Kalman gain

$$\mathbf{K}_t = \mathbf{B}_t \mathbf{F}_t^T Q_t^{-1}, \quad (6)$$

with $\mathbf{B}_t = \text{cov}[\boldsymbol{\theta}_t \mid \mathbf{y}_{1:t-1}]$ and $Q_t = \text{var}[y_t \mid \mathbf{y}_{1:t-1}]$ from the Kalman filter in (26) and (27) in Appendix A, respectively. Then $\tilde{\mathbf{x}} = \mathbf{L}^T \mathbf{u}$.

Lemma 2 (Compute $\mathbf{x} = \mathbf{L} \tilde{\mathbf{x}}$ with linear computational cost). *For any N -dimensional vector $\tilde{\mathbf{x}}$, let $x_1 = \mathbf{F}_1 \mathbf{b}_1 + Q_1^{1/2} \tilde{x}_1$ and $\tilde{\mathbf{m}}_1 = \mathbf{b}_1 + \mathbf{K}_1(x_1 - \mathbf{F}_1 \mathbf{b}_1)$. For $t = 2, \dots, N$, iteratively compute x_t by*

$$\mathbf{b}_t = \mathbf{G}_t \tilde{\mathbf{m}}_{t-1}, \quad (7)$$

$$x_t = \mathbf{F}_t \mathbf{b}_t + Q_t^{\frac{1}{2}} \tilde{x}_t, \quad (8)$$

$$\tilde{\mathbf{m}}_t = \mathbf{b}_t + \mathbf{K}_t(x_t - \mathbf{F}_t \mathbf{b}_t), \quad (9)$$

where Q_t and \mathbf{K}_t are from (27) and (6), respectively. Then $\mathbf{x} = \mathbf{L} \tilde{\mathbf{x}}$.

The algorithm in Lemma 1 is unconventional and nontrivial to derive. In contrast, Lemma 2 has a direct connection to the Kalman filter. Specifically, the one-step-ahead predictive distribution in step (ii) of the Kalman filter, given in Appendix A, enables computing $\mathbf{L}^{-1} \mathbf{x}$ for any vector \mathbf{x} (Lemma A2). Lemma 2 essentially reverses this operation, computing $\mathbf{L} \tilde{\mathbf{x}}$ for any vector $\tilde{\mathbf{x}}$, leading to the term *Inverse Kalman filter* (IKF).

The IKF algorithm, outlined in Algorithm 1, sequentially applies Lemmas 1 and 2 to reduce the computational cost and storage for $\Sigma \mathbf{u}$ from $\mathcal{O}(N^2)$ to $\mathcal{O}(q^3 N)$ without approximation. The IKF applies to all DLMS, including Gaussian processes that admit equivalent DLM representation, such as Gaussian processes with Matérn kernels where roughness parameters 0.5 and 2.5 correspond to $q = 1$ and $q = 3$, respectively. Details are provided in the Supplementary Material.

While Algorithm 1 can be applied to DLM regardless of the noise variance, we do not recommend directly computing $\Sigma \mathbf{u}$ in scenarios when the noise variance V_t is zero or close to zero in Eq. (1). This

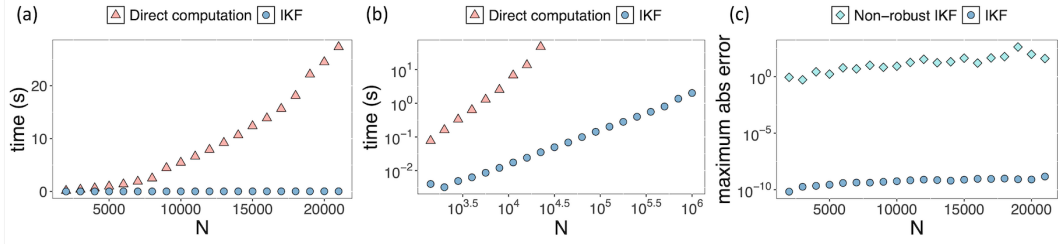


Figure 2: Panels (a) and (b) compare the IKF (blue dots) with direct computation (red triangles) for computing $\Sigma \mathbf{u}$ in the original time scale and logarithmic scale (base 10), respectively. Panel (c) shows the predictive error comparison between the non-robust IKF (light blue squares) and the robust IKF (blue dots).

is because when $V_t = 0$, Q_t in Eq. (27), the variance of the one-step-ahead predictive distribution, could be extremely small, which leads to large numerical errors in Eq. (28) due to unstable inversion of Q_t . To ensure robustness, we suggest computing $\mathbf{x} = (\Sigma + V\mathbf{I}_N)\mathbf{u}$ with a positive scalar V and outputting $\mathbf{x} - V\mathbf{u}$ as the result of $\Sigma \mathbf{u}$. Here, $\Sigma + V\mathbf{I}_N$ can be interpreted as the covariance matrix of a DLM with noise variance $V_t = V$. Essentially, we introduce artificial noise to ensure that Q_t computed in KF is at least V for numerical stability. The result remains exact and independent of the choice of V .

We compare the IKF approach with the direct matrix-vector multiplication of $\Sigma \mathbf{u}$ in noise-free scenarios in Fig. 2. The experiments utilize $z_t = z(d_t)$ with d uniformly sampled from $[0, 1]$ and the Matérn covariance with unit variance, roughness parameter 2.5, and range parameter $\gamma = 0.1$ [13]. Panels (a) and (b) show that the IKF significantly reduces computational costs compared to direct computation. The IKF achieves covariance matrix-vector multiplication for an output vector of 10^6 dimensions in about 2 seconds on a desktop, making it highly scalable for iterative algorithms like the conjugate gradient algorithm [16] and the randomized log-determinant approximation [30]. Fig. 2(c) compares the maximum absolute error between the robust IKF with $V = 0.1$ and the non-robust IKF with $V = 0$. The non-robust IKF exhibits large numerical errors due to instability when Q_t approaches zero, while the robust IKF remains stable by ensuring Q_t is no smaller than V , even with near-singular covariance matrices Σ .

Lemmas 1 and 2 facilitate the computation of each element in \mathbf{L} using DLM parameters and enable the linear computation of $(\mathbf{L}^T)^{-1}\tilde{\mathbf{x}}$. These results are summarized in Lemmas 3 and 4, respectively, with proofs provided in the Supplementary Material.

Lemma 3 (Cholesky factor from the inverse Kalman filter). *Each entry (t', t) in the lower triangular matrix \mathbf{L} with $t' \geq t$ has the form*

$$L_{t',t} = Q_t^{\frac{1}{2}} \ell_{t',t}, \quad (10)$$

where $\ell_{t',t} = 1$, and for $t' > t$, $\ell_{t',t}$ is defined as

$$\ell_{t',t} = \mathbf{F}_{t'} \left(\prod_{l=t+1}^{t'} \mathbf{G}_l \right) \mathbf{K}_t, \quad (11)$$

with $\prod_{l=t+1}^{t'} \mathbf{G}_l = \mathbf{G}_{t'} \mathbf{G}_{t'-1} \dots \mathbf{G}_{t+1}$, Q_t and \mathbf{K}_t defined in (27) and (6), respectively.

Lemma 4 (Compute $\mathbf{u} = (\mathbf{L}^T)^{-1}\tilde{\mathbf{x}}$ with linear computational cost). *For any $\tilde{\mathbf{x}}$, let $u_N = Q_N^{-1/2}\tilde{x}_N$,*

and $u_{N-1} = Q_{N-1}^{-1/2} \tilde{x}_{N-1} - \ell_{N,N-1} u_N$. For $t = N-2, \dots, 1$, iteratively compute u_t by

$$u_t = Q_t^{-\frac{1}{2}} \tilde{x}_t - \tilde{\ell}_{t+1,t} - \ell_{t+1,t} u_{t+1}, \quad (12)$$

with $\tilde{\ell}_{t+1,t}$ and $\ell_{t+1,t}$ defined in Lemma 1. Then $\mathbf{u} = (\mathbf{L}^T)^{-1} \tilde{\mathbf{x}}$.

3 Nonparametric estimation of particle interaction functions

The IKF algorithm is motivated by the problem of estimating interactions between particles, which is crucial to understanding complex behaviors of molecules and active matter, such as migrating cells and flocking birds. Minimal physical models, such as the Vicsek model [36] and their extensions [1, 9], provide a framework for explaining the collective motion of active matter.

Consider a physical model encompassing multiple types of latent interactions. Let \mathbf{y}_i be a D_y -dimensional output vector corresponding to particle i' at time τ , which is influenced by J distinct interaction types. For the j th type of interaction, the i th observational vector interacts with a subset $p_{i,j}$ of particles rather than with all particles, typically those within a radius r_j . This relationship is expressed as a latent factor model:

$$\mathbf{y}_i = \sum_{j=1}^J \sum_{k=1}^{p_{i,j}} \mathbf{a}_{i,j,k} z_j(d_{i,j,k}) + \boldsymbol{\epsilon}_i, \quad (13)$$

where $\boldsymbol{\epsilon}_i \sim \mathcal{MN}(0, \sigma_0^2 I_{D_y})$ denotes a Gaussian noise vector. The term $\mathbf{a}_{i,j,k}$ is a D_y -dimensional *known* factor loading that links the i th output to the k th neighbor in the j th interaction, with the *unknown* interaction function $z_j(\cdot)$ evaluated at a scalar-valued input $d_{i,j,k}$, such as the distance between particles i' and k , for $k = 1, \dots, p_{i,j}$, $i = 1, \dots, n$, and $j = 1, \dots, J$. For a dataset of n_p particles over n_τ time points, the total number of observations is $\tilde{N} = n D_y = n_p n_\tau D_y$.

An illustrative example of this framework is an unnormalized Vicsek model. Unlike the original Vicsek model [36], which enforces a constant speed for all particles, we allow velocity magnitudes to vary over time. Time-varying velocities are more sensible in many real-world scenarios, including cellular movements studied in Section 4.4. When the system approaches a high degree of confluence, the average velocity of the cells typically decreases because of cell proliferation. The 2-dimensional velocity of the i' th particle at time τ , $\mathbf{v}_{i'}(\tau) = (v_{i',1}(\tau), v_{i',2}(\tau))^T$, is updated by averaging the velocity of its neighbors from the previous time step. Specifically, for each direction $l = 1, 2$,

$$v_{i',l}(\tau) = \frac{1}{p_{i'}(\tau-1)} \sum_{k \in ne_{i'}(\tau-1)} v_{k,l}(\tau-1) + \epsilon_{i',l}(\tau), \quad (14)$$

where $\epsilon_{i'}(\tau)$ is a zero-mean Gaussian noise with variance σ_0^2 . The set of neighbors $ne_{i'}(\tau-1)$ includes particles within a radius of r from particle i' at time $\tau-1$, i.e., $ne_{i'}(\tau-1) = \{k : \|\mathbf{s}_{i'}(\tau-1) - \mathbf{s}_k(\tau-1)\| < r\}$, where $\mathbf{s}_{i'}(\tau-1)$ and $\mathbf{s}_k(\tau-1)$ are 2-dimensional position vectors of particle i' and its neighbor k , respectively, and $p_{i'}(\tau-1)$ denotes the total number of neighbors of the i' th particle, including itself, at time $\tau-1$. The illustration of this model is shown in Fig. S1(b) in the Supplementary Material.

The unnormalized Vicsek model in Eq. (14) is a special case of the general framework in Eq. (13) with scalar output $\mathbf{y}_i = v_{i',l}(\tau)$, i.e. $D_y = 1$, and the index of the i th observation $i = (\tau-1)n_p + i'$ is a function of time τ and particle i' . This model contains a single interaction, i.e. $J = 1$, with a linear interaction function $z(d) = d$, where d is the velocity component of the neighboring particle, and the factor loading being $1/p_{i'}(\tau-1)$.

Numerous other physical models of self-propelled particles can also be formulated as in Eq. (13) with a parametric form of a particle interaction function [1]. Nonparametric estimation of particle interactions is preferred when the physical mechanism is unknown [18, 24], but the high computational cost limits its applicability to systems with large numbers of particles over long time periods.

In this work, we model each latent interaction function $z_j(\cdot)$ nonparametrically using a Gaussian process. By utilizing an equivalent DLM representation, we can leverage the proposed IKF algorithm to significantly expedite computation. This includes commonly used kernels such as Matérn kernel with a half-integer roughness parameter [13], often used as the default setting for Gaussian process models to predict nonlinear functions, as the smoothness of the process can be controlled by its roughness parameters [12].

For each interaction j , we form the input vector $\mathbf{d}_j^{(u)} = [d_{1,j}^{(u)}, \dots, d_{N_j,j}^{(u)}]^T$, where ‘u’ indicates that the input entries are unordered, $d_{t,j}^{(u)} = d_{i,j,k}$ with $t = \sum_{i'=1}^{i-1} p_{i',j} + k$ for any tuple (i, j, k) , $k = 1, \dots, p_{i,j}$, $i = 1, \dots, n$, $j = 1, \dots, J$, and $N_j = \sum_{i=1}^n p_{i,j}$. The marginal distribution of the j th factor follows $\mathbf{z}_j^{(u)} = [z_j(d_{1,j}^{(u)}), \dots, z_j(d_{N_j,j}^{(u)})]^T \sim \mathcal{MN}(\mathbf{0}, \mathbf{\Sigma}_j^{(u)})$, where the (t, t') th entry of the $N_j \times N_j$ covariance matrix $\mathbf{\Sigma}_j^{(u)}$ is $\text{cov}[z_j(d_{t,j}^{(u)}), z_j(d_{t',j}^{(u)})] = \sigma_j^2 c_j(d_{t,j}^{(u)}, d_{t',j}^{(u)}) = \sigma_j^2 c_j(d)$, with $d = |d_{t,j}^{(u)} - d_{t',j}^{(u)}|$, σ_j^2 and $c_j(\cdot)$ being the variance parameter and the correlation function, respectively. We employ the Matérn correlation with roughness parameters $\nu_j = 0.5$ and $\nu_j = 2.5$. For $\nu_j = 0.5$, the Matérn correlation is the exponential correlation $c_j(d) = \exp(-d/\gamma_j)$, while for $\nu_j = 2.5$, the Matérn correlation follows:

$$c_j(d) = \left(1 + \frac{5^{1/2}d}{\gamma_j} + \frac{5d^2}{3\gamma_j^2}\right) \exp\left(-\frac{5^{1/2}d}{\gamma_j}\right), \quad (15)$$

where γ_j denotes the range parameter.

By integrating out latent factor processes \mathbf{z}_j , the marginal distribution of the observational vector $\mathbf{y} = (\mathbf{y}_1^T, \dots, \mathbf{y}_n^T)^T$, with dimension $\tilde{N} = nD_y$, follows a multivariate normal distribution:

$$(\mathbf{y} \mid \mathbf{\Sigma}_j^{(u)}, \sigma_0^2) \sim \mathcal{MN}\left(\mathbf{0}, \sum_{j=1}^J \mathbf{A}_j \mathbf{\Sigma}_j^{(u)} \mathbf{A}_j^T + \sigma_0^2 \mathbf{I}_{\tilde{N}}\right), \quad (16)$$

where \mathbf{A}_j is a sparse $\tilde{N} \times N_j$ block diagonal matrix, such that the i th diagonal block is a $D_y \times p_{i,j}$ matrix $\mathbf{A}_{i,j} = [\mathbf{a}_{i,j,1}, \dots, \mathbf{a}_{i,j,p_{i,j}}]$ for $i = 1, \dots, n$. The posterior predictive distribution of the latent variable $z_j(d^*)$ for any given input d^* is also a normal distribution:

$$(z_j(d^*) \mid \mathbf{y}, \sigma_0^2, \sigma^2, \gamma, \mathbf{r}) \sim \mathcal{N}(\hat{z}_j(d^*), c_j^*(d^*)), \quad (17)$$

with the predictive mean and variance given by

$$\hat{z}_j(d^*) = \mathbf{\Sigma}_j^{(u)}(d^*)^T \mathbf{A}_j^T \mathbf{\Sigma}_y^{-1} \mathbf{y}, \quad (18)$$

$$c_j^*(d^*) = c_j(d^*, d^*) - \mathbf{\Sigma}_j^{(u)}(d^*)^T \mathbf{A}_j^T \mathbf{\Sigma}_y^{-1} \mathbf{A}_j \mathbf{\Sigma}_j^{(u)}(d^*), \quad (19)$$

where $\mathbf{\Sigma}_y = \sum_{j=1}^J \mathbf{A}_j \mathbf{\Sigma}_j^{(u)} \mathbf{A}_j^T + \sigma_0^2 \mathbf{I}_{\tilde{N}}$, $\mathbf{\Sigma}_j^{(u)}(d^*) = [c_j(d_{1,j}^{(u)}, d^*), \dots, c_j(d_{N_j,j}^{(u)}, d^*)]^T$, and \mathbf{r} represents additional system parameters.

The main computational challenge in calculating the predictive distribution in (17) lies in inverting the covariance matrix $\mathbf{\Sigma}_y$, where \tilde{N} and N_j range between 10^5 and 10^6 in our applications. Though various Gaussian process approximation methods have been proposed [35, 31, 8, 2, 23, 10,

3, 19], they typically approximate the parametric covariance $\Sigma_j^{(u)}$ rather than Σ_y , thus not directly applicable for computing the distribution in (17).

To address this, we employ the conjugate gradient (CG) algorithm [16] to accelerate the computation of the predictive distribution. Each conjugate gradient iteration needs to compute $\Sigma_y \mathbf{u}$ for an \tilde{N} -dimensional vector \mathbf{u} . To employ the IKF, we first rearrange the input vector $\mathbf{d}_j^{(u)}$ into a non-decreasing input sequence $\mathbf{d}_j = [d_{1,j}, \dots, d_{N_j,j}]^T$. Denote the covariance $\text{var}[\mathbf{z}_j] = \Sigma_j$ with $\mathbf{z}_j = [z_j(d_{1,j}), \dots, z_j(d_{N_j,j})]^T$. The covariance of the observations can be written as a weighted sum of Σ_j by introducing a permutation matrix for each interaction: $\Sigma_y = \sum_{j=1}^J \mathbf{A}_{\pi,j} \Sigma_j \mathbf{A}_{\pi,j}^T + \sigma_0^2 \mathbf{I}_N$, where $\mathbf{A}_{\pi,j} = \mathbf{A}_j \mathbf{P}_j^T$ with \mathbf{P}_j being a permutation matrix such that $\Sigma_j = \mathbf{P}_j \Sigma_j^{(u)} \mathbf{P}_j^T$. After this reordering, the computation of $\Sigma_y \mathbf{u}$ can be broken into four steps: (1) $\mathbf{u}_j = \mathbf{A}_{\pi,j}^T \mathbf{u}$, (2) $\mathbf{x}_j = \Sigma_j \mathbf{u}_j$, (3) $\hat{\mathbf{u}}_j = \mathbf{A}_{\pi,j} \mathbf{x}_j$, and (4) $\sum_{j=1}^J \hat{\mathbf{u}}_j + \sigma_0^2 \mathbf{u}$. Here, \mathbf{A}_j is a sparse matrix with $N_j D_y$ non-zero entries. The IKF algorithm is used in step (2) to accelerate the most expensive computation, with all computations performed directly using terms in the KF algorithm without explicitly constructing the covariance matrix.

We refer to the resulting approach as the IKF-CG algorithm. This approach reduces the computational cost for computing the posterior distribution from $\mathcal{O}(\tilde{N}^3)$ operations to pseudolinear order with respect to N_j , as shown in Table S1 in the Supplementary Material. Furthermore, the IKF-CG algorithm can accelerate the parameter estimation via both cross-validation and maximum likelihood estimation, with the latter requiring an additional approximation of the log-determinant [30]. Details of the conjugate gradient algorithm, the computation of the predictive distribution, parameter estimation procedures, and computational complexity are discussed in Sections S3, S4, S6, and S7 of the Supplementary Material, respectively.

4 Numerical results for particle interaction function estimation

4.1 Evaluation criteria

We conduct simulation studies in Sections 4.2-4.3 and analyze real cell trajectory data in Section 4.4 to estimate particle interaction functions in physical models. The code and data to reproduce all numerical results are available at <https://github.com/UncertaintyQuantification/IKF>. We have implemented the main functions of the IKF and IKF-CG algorithms for estimating particle interaction functions in the **FastGaSP** package on CRAN [11]. The observations in simulation are generated at equally spaced time frames $\tau = 1, \dots, n_\tau$ with interval $h = 0.1$, though the proposed approach is applicable to both equally and unequally spaced time frames. For simplicity, the number of particles n_p is assumed constant across all time frames during simulations.

For each of the J latent factors, predictive performance is assessed using normalized root mean squared error (NRMSE_j), the average length of the 95% posterior credible interval ($L_j(95\%)$), and the proportion of interaction function values covered within the 95% posterior credible interval

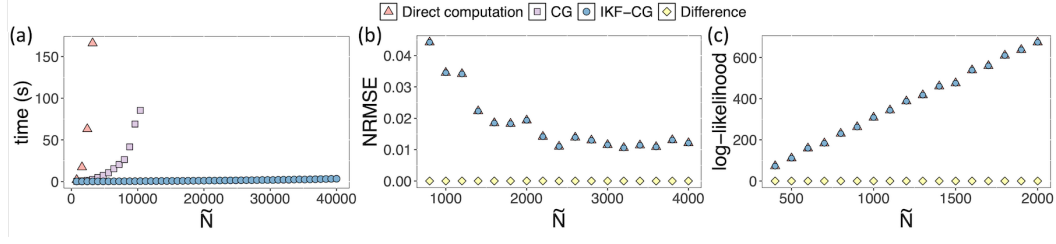


Figure 3: (a) Computational time of calculating predictive means using IKF-CG algorithm (blue dots), CG method (purple squares), and direct computation (red triangles) for the unnormalized Vicsek model with different numbers of observations. (b, c) NRMSE of predictive means for interaction function and log-likelihood comparing direct computation (red triangles) and IKF-CG algorithm (blue dots), with differences (yellow diamonds) of order 10^{-7} to 10^{-5} and 10^{-5} to 10^{-4} , respectively.

$(P_j(95\%))$, based on n^* test inputs $\mathbf{d}_j^* = (d_{1,j}^*, \dots, d_{n^*,j}^*)^T$:

$$\text{NRMSE}_j = \left(\frac{\sum_{i=1}^{n^*} (\hat{z}_j(d_{i,j}^*) - z_j(d_{i,j}^*))^2}{\sum_{i=1}^{n^*} (\bar{z}_j - z_j(d_{i,j}^*))^2} \right)^{1/2}, \quad (20)$$

$$L_j(95\%) = \frac{1}{n^*} \sum_{i=1}^{n^*} \text{length} \{CI_{i,j}(95\%)\}, \quad (21)$$

$$P_j(95\%) = \frac{1}{n^*} \sum_{i=1}^{n^*} 1_{z_j(d_{i,j}^*) \in CI_{i,j}(95\%)}. \quad (22)$$

Here, $\hat{z}_j(d_{i,j}^*)$ represents the predicted mean at $d_{i,j}^*$, \bar{z}_j is the average of the j th interaction function, and $CI_{i,j}(95\%)$ denotes the 95% posterior credible interval of $z_j(d_{i,j}^*)$, for $j = 1, \dots, J$. A desirable method should have a low NRMSE_j , small $L_j(95\%)$, and $P_j(95\%)$ close to 95%.

To account for variability due to initial particle positions, velocities, and noise, each simulation scenario is repeated $E = 20$ times to compute the average performance metrics. Unless otherwise specified, parameters are estimated by cross-validation, with 80% of the data used as a training set and the rest 20% as the validation set. All computations are performed on a macOS Mojave system with an 8-core Intel i9 processor running at 3.60 GHz and 32 GB of RAM.

4.2 Unnormalized Vicsek model

We first consider the unnormalized Vicsek model introduced in Section 3. For each particle i' at time τ , after obtaining its velocity using Eq. (14), its position is updated as:

$$\mathbf{s}_{i'}(\tau) = \mathbf{s}_{i'}(\tau - 1) + \mathbf{v}_{i'}(\tau)h, \quad i = 1', \dots, n_p, \quad (23)$$

where h is the time step size. Particles are initialized with velocity $[v \cos(\phi_{i'}(0)), v \sin(\phi_{i'}(0))]^T$, where $\phi_{i'}(0)$ is drawn from $\text{Unif}[-\pi, \pi]$ and $v = 2^{1/2}/2 \approx 0.71$. Initial particle positions $\mathbf{s}_{i'}(0)$ are uniformly sampled from $[0, n_p^{1/2}] \times [0, n_p^{1/2}]$ to keep consistent particle density across experiments. The goal is to estimate the interaction function nonparametrically, without assuming linearity. The interaction radius $r = 0.5$ is estimated alongside other parameters, with results detailed in the Supplementary Material.

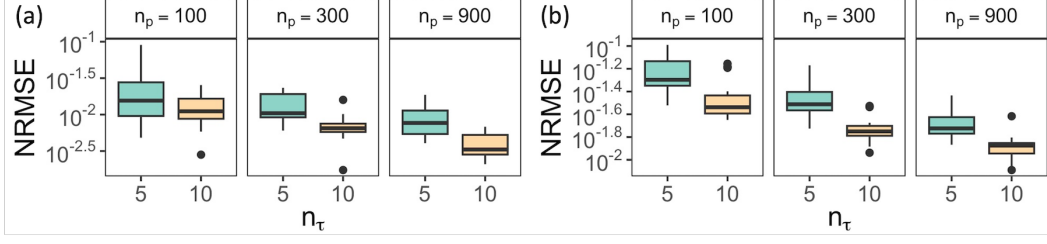


Figure 4: Boxplots of NRMSE (Eq. (20)) for estimating the latent interaction function in the unnormalized Vicsek model with $\sigma_0^2 = 0.1^2$ based on 20 experiments. Panel (a) uses the Matérn covariance with roughness parameter 2.5, and panel (b) uses the exponential covariance.

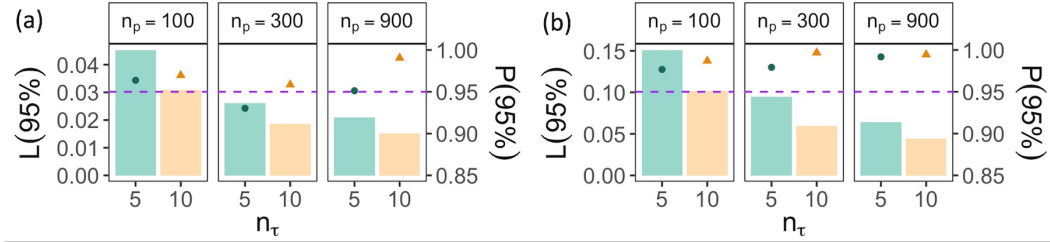


Figure 5: Uncertainty assessment of predicted interaction function in the unnormalized Vicsek model with $\sigma_0^2 = 0.1^2$ using (a) Matérn covariance function in Eq. (15) and (b) exponential covariance function. Bars represent average lengths of 95% posterior credible intervals (Eq. (21)). Dots indicate the proportions covered in the 95% intervals (Eq. (22)), with optimal coverage (0.95) shown as the purple dashed line.

We first compare the computational cost and accuracy of IKF-CG, CG, and direct computation for calculating the predictive mean in Eq. (18) and the marginal likelihood in Eq. (16) using the covariance in Eq. (15). Simulations are conducted with $n_p = 100$ particles and noise variance $\sigma_0^2 = 0.2^2$. Panel (a) of Fig. 3 shows that the IKF-CG approach substantially outperforms both direct computation and the CG algorithm in computational time when predicting $n^* = 100$ test inputs with varying time lengths n_τ , ranging from 4 to 200. Figure 3(b) compares the NRMSE of the predictive mean between the direct computation and IKF-CG method when the number of observations ranges from 400 to 2,000, corresponding to n_τ from 4 to 20. The two methods yield nearly identical predictive errors, with negligible differences in NRMSE. Figure 3(c) shows a comparison of the log-likelihood values computed via direct computation and IKF-CG, where the latter employs the log-determinant approximation detailed in the Supplementary Material. Both methods produce similar log-likelihood values across different sample sizes.

Next, we evaluate the performance of the IKF-CG algorithm across 12 scenarios with varying particle numbers ($n_p = 100, 300, 900$), time frames ($n_\tau = 5, 10$), and noise variances ($\sigma_0^2 = 0.1^2, 0.2^2$). The predictive performance is evaluated using $n^* = 200$ test velocity inputs evenly spaced across a representative input domain of the interaction function in the data, $[-1, 1]$, averaged over $E = 20$ experiments.

Panels (a) and (b) of Figs. 4-5 show the predictive performance of particle interactions using the Matérn covariance with roughness parameter $\nu = 2.5$ and the exponential covariance (Matérn with $\nu = 0.5$), respectively, for noise variance $\sigma_0^2 = 0.1^2$. Results for $\sigma_0^2 = 0.2^2$ are provided in the Supplementary Material. Across all scenarios, NRMSEs remain low, with improved accuracy for larger datasets and smaller noise variances. The decrease in the average length of the 95% posterior

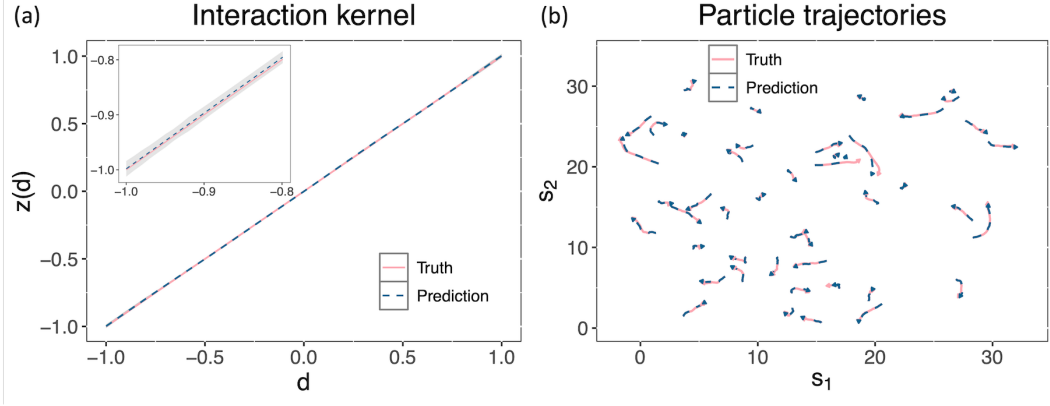


Figure 6: (a) Predicted (blue dashed lines) and true (pink solid lines) interaction functions with 95% posterior credible interval (grey shaded area) for the unnormalized Vicsek model with $n_\tau = 900$, $T = 10$, and $\sigma_0^2 = 0.1^2$, using Matérn covariance function with $\nu = 2.5$. (b) Trajectories of 45 sample particles over 50 time frames using estimated (blue dashed lines) and true (pink solid lines) interaction functions with identical initial positions and noise samples.

credible interval with increasing sample size, along with the relatively small interval span compared to the output range, indicates improved prediction confidence with more observations. Moreover, the coverage proportion for the 95% posterior credible interval is close to the nominal 95% level in all cases, validating the reliability of the uncertainty quantification. By comparing panels (a) and (b) in Figs. 4-5, we find that the Matérn covariance in Eq. (15) yields lower NRMSE and narrower 95% posterior credible intervals than the exponential kernel. This improvement is due to the smoother latent process induced by Eq. (15), which is twice mean-squared differentiable, while the process with an exponential kernel is not differentiable.

Figure 6(a) shows close agreement between predicted and true interaction functions. The 95% posterior credible interval is narrow yet covers approximately 95% of the test samples of the interaction function. Figure 6(b) compares particle trajectories over 50 time steps by the predicted mean of one-step-ahead predictions and the true interaction function, both having the same noise vectors. The trajectories are visually similar.

4.3 A modified Vicsek model with multiple interactions

Various extensions of the Vicsek model have been studied to capture more complex particle dynamics [1, 9]. For illustration, we consider a modified Vicsek model with two interaction functions. The 2-dimensional velocity $\mathbf{v}_{i'}(\tau) = (v_{i',1}(\tau), v_{i',2}(\tau))^T$, corresponding to the output in Eq. (13), is updated according to:

$$\mathbf{v}_{i'}(\tau) = \frac{\sum_{k \in ne_{i'}(\tau-1)} \mathbf{v}_k(\tau-1)}{p_{i'}(\tau-1)} + \frac{\sum_{k \in ne'_{i'}(\tau-1)} f(d_{i',k}(\tau-1)) \mathbf{e}_{i',k}(\tau-1)}{p'_{i'}(\tau-1)} + \boldsymbol{\epsilon}_{i'}(\tau), \quad (24)$$

where $\boldsymbol{\epsilon}_{i'}(\tau) = (\epsilon_{i',1}(\tau), \epsilon_{i',2}(\tau))^T$ is a Gaussian noise vector with variance σ_0^2 and $D_y = 2$. The first term in (24) models velocity alignment with neighboring particles, and the second term introduces a distance-dependent interaction function $f(\cdot)$. The definitions of neighbor sets, 2-dimensional vector $\mathbf{e}_{i',k}(\tau-1)$, and the second interaction function $f(\cdot)$ are provided in Section S8.2 of the Supplementary Material.

		First Interaction			Second Interaction		
		NRMSE	$L_1(95\%)$	$P_1(95\%)$	NRMSE	$L_2(95\%)$	$P_2(95\%)$
$n_p = 100$	$n_\tau = 5$	6.8×10^{-3}	0.098	92%	8.7×10^{-2}	0.29	94%
	$n_\tau = 10$	6.0×10^{-3}	0.097	95%	3.8×10^{-2}	0.18	96%
$n_p = 300$	$n_\tau = 5$	1.2×10^{-2}	0.23	87%	3.2×10^{-2}	0.21	96%
	$n_\tau = 10$	4.2×10^{-3}	0.10	98%	2.0×10^{-2}	0.13	97%
$n_p = 900$	$n_\tau = 5$	5.6×10^{-3}	0.10	96%	1.4×10^{-2}	0.12	98%
	$n_\tau = 10$	4.4×10^{-3}	0.12	97%	1.4×10^{-2}	0.10	96%

Table 1: The predictive accuracy and uncertainty assessment by (20)-(22) for the modified Vicsek model with $\sigma_0^2 = 0.1^2$ using Matérn covariance function and roughness parameter 2.5.

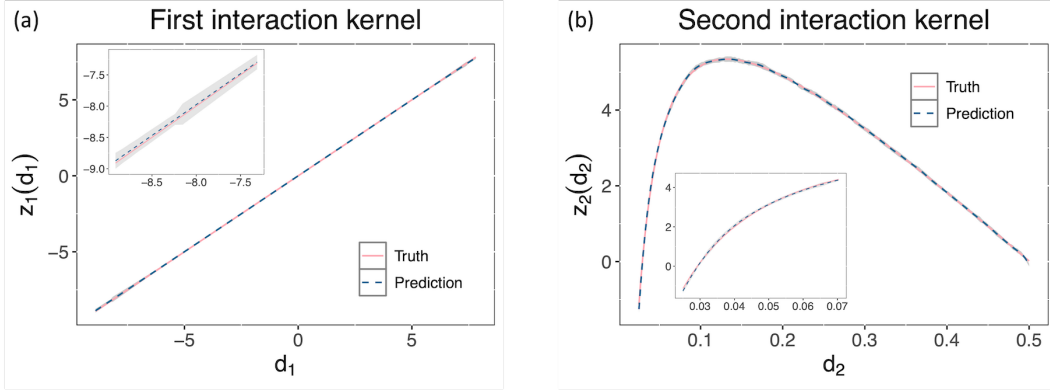


Figure 7: Predictions (blue dashed curves), truth (pink solid curves), and the 95% posterior credible interval (shaded region) of particle interaction functions when $n_p = 900$, $n_\tau = 10$, and $\sigma_0^2 = 0.1^2$.

We simulate 12 scenarios, each replicated $E = 20$ times, using the same number of particles, time frame, and noise level as in the unnormalized Vicsek model in Section 4.2. The predictive performance of the IKF-CG is evaluated using $n^* = 200$ test inputs evenly spaced across the input domain of each interaction function. We focus on the model with the Matérn kernel in Eq. (15), and results for the exponential kernel are detailed in the Supplementary Material. Consistent with the results of the unnormalized Vicsek model, we find models with the Matérn kernel in Eq. (15) are more accurate due to the smooth prior imposed on the interaction function.

Table 1 summarizes the predictive performance for $\sigma_0^2 = 0.1^2$; results for $\sigma_0^2 = 0.2^2$ are included in the Supplementary Material. While both interaction functions exhibit relatively low NRMSEs, the second interaction function has a higher NRMSE than the first, because the repulsion at short distances creates fewer training samples with close-proximity neighbors. This discrepancy can be mitigated by increasing the number of observations. The average length of the 95% posterior credible interval for the second interaction decreases as the sample size increases, and the coverage proportion remains close to the nominal 95% level across all scenarios.

In Fig. 7, we show the predictions of the interaction functions, where the shaded regions represent the 95% posterior credible intervals. The input velocities are larger than the unnormalized Vicsek model due to the inclusion of the second interaction function, and thus the test input domain in Fig. 7(a) is wider than that in Fig. 6(a). The predictions closely match the true values, and the credible intervals, while narrow relative to the output range and nearly invisible in the plots, mostly cover the truth. These results suggest high confidence in the predictions.

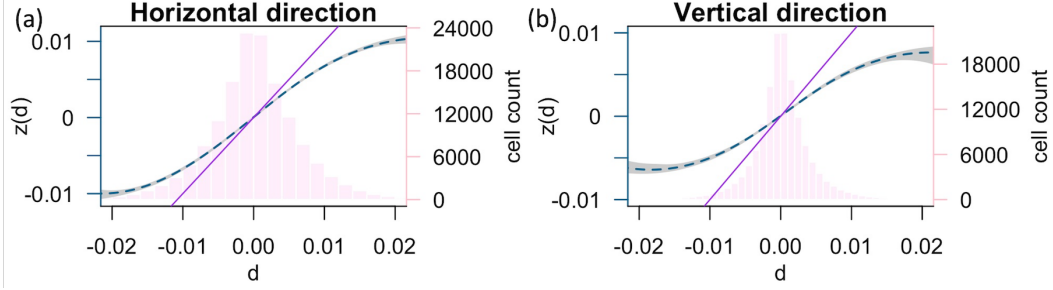


Figure 8: The blue dashed curves show the predicted interaction function for the horizontal and vertical directions. The grey shaded area is the 95% posterior credible interval. The purple line of slope 1 is the prediction using the unnormalized Vicsek model. The light pink histogram shows the velocity distribution of all training samples.

4.4 Estimating cell-cell interactions on anisotropic substrates

We analyze video microscopy data from [25], which tracks the trajectories of over 2,000 human dermal fibroblasts moving on a nematically aligned, liquid-crystalline substrate. This experimental setup encourages cellular alignment along a horizontal axis, with alignment order increasing over time, though the underlying mechanism remains largely unknown. Cells were imaged every 20 minutes over a 36-hour period, during which the cell count grew from 2,615 to 2,953 due to proliferation. Our objective is to estimate the latent interaction function between cells. Given the vast number of velocity observations ($N \approx 300,000$), direct formation and inversion of the covariance matrix is impractical.

We apply the IKF-CG algorithm to estimate the latent interaction function. Due to the anisotropic substrate, cellular velocities differ between horizontal and vertical directions, so we independently model the velocity of the i' th cell in each direction l by

$$v_{i',l}(\tau) = \frac{1}{p_{ne_{i',l}(\tau-1)}} \sum_{k \in ne_{i',l}(\tau-1)} z_l(d_{k,l}) + \epsilon_{i',l}(\tau), \quad i' = 1, \dots, n_p(\tau) \quad (25)$$

where $n_p(\tau)$ is the cell count at time τ , $l = 1, 2$ correspond to horizontal and vertical directions, respectively, and $\epsilon_{i',l}(\tau) \sim \mathcal{N}(0, \sigma_{0,l}^2(\tau))$ denotes the noise. Inspired by the modified Vicsek model, we set $d_{k,l} = v_{k,l}(\tau - 1)$. To account for velocity decay caused by increasing cell confluence, we model the noise variances as $\sigma_{0,l}^2(\tau) = \omega_l \sigma_{v,l}^2(\tau - 1)$, where $\sigma_{v,l}^2(\tau - 1)$ is the sample velocity variance at time $(\tau - 1)$, and ω_l is a parameter estimated from data for $l = 1, 2$. The neighboring set $ne_{i',l}(\tau - 1) = \{k : \|\mathbf{s}_{i'}(\tau - 1) - \mathbf{s}_k(\tau - 1)\| < r_l \text{ and } \mathbf{v}_{i'}(\tau - 1)^T \mathbf{v}_k(\tau - 1) > 0\}$, where r_l denotes the interaction radius of direction l for $l = 1, 2$, excludes particles moving in opposite directions, reflecting the observed gliding and intercalating behavior of cells [37].

We use observations from the first half of the time frames as the training set and the latter half as the testing set. The predicted interaction functions in Fig. 8 show diminishing effects in both directions, likely due to cell-substrate interactions such as friction. The estimated uncertainty (obtained via residual bootstrap) increases when the absolute velocity of neighboring cells in the previous time frame is large, which is attributed to fewer observations at the boundaries of the input domain. Furthermore, the interaction in the vertical direction is weaker than in the horizontal direction, due to the confinement from the anisotropic substrate in the vertical direction.

Our nonparametric estimation of the interaction functions is compared with two models for one-step-ahead forecasts of directional velocities: the unnormalized Vicsek model introduced in Section

	Horizontal direction			Vertical direction		
	RMSE	L(95%)	P(95%)	RMSE	L(95%)	P(95%)
Unnormalized Vicsek	3.9×10^{-3}	0.029	99%	2.6×10^{-3}	0.029	99%
Anisotropic Vicsek	3.9×10^{-3}	0.034	99%	2.6×10^{-3}	0.022	99%
Nonparametric estimation	3.5×10^{-3}	0.015	95%	2.3×10^{-3}	0.0092	95%

Table 2: One-step-ahead prediction performance on the testing dataset. Here $\text{RMSE} = \{\sum_{\tau=1}^{n_{\tau}^*} \sum_{i'=1}^{n_p(\tau)} (\hat{v}_{i',l}(\tau) - v_{i',l}(\tau))^2 / \sum_{\tau=1}^{n_{\tau}^*} n_p(\tau)\}^{1/2}$, with n_{τ}^* denoting the number of testing time frames. L(95%) and P(95%) are computed similarly to those in Eqs. (21) - (22), but with the predictive interval of z replaced by that of y , where y represents the velocity in each direction.

4.2, which uses a shared interaction radius for both velocity components, and the anisotropic Vicsek model, which uses distinct radii in each direction. As shown in Table 2, both Vicsek models have similar RMSE as the difference of interaction radii does not have a large impact for estimating interaction functions. Our model outperforms both Vicsek models in RMSE for one-step-ahead forecasts of directional velocities, despite the large inherent stochasticity in cellular motion. Moreover, our model has notably shorter average interval lengths that cover approximately 95% of the held-out observations. These findings underscore the importance of the IFK-CG algorithm in enabling the use of large datasets to overcome high stochasticity and capture the underlying dynamics of cell alignment processes.

5 Concluding remarks

Several future directions are worth exploring. First, computing large matrix-vector products is ubiquitous, and the approach can be extended to different models, including some large neural network models. Second, it is an open topic to scalably compute the logarithm of the determinant of the covariance in Eq. (3) without approximation. Third, the new approach can be extended to estimate latent functions when forward equations are unavailable or computationally intensive in nonlinear or non-Gaussian dynamical systems, where ensemble Kalman filter [6, 34] and particle filter [21] are commonly used. Fourth, our approach can be extended for estimating and predicting multivariate time series [22] and generalized factor processes for categorical observations [4]. Finally, we aim to generalize the fast approach to scenarios with input dimensions larger than one.

Acknowledgement

Xinyi Fang acknowledges partial support from the BioPACIFIC Materials Innovation Platform of the National Science Foundation under Award No. DMR-1933487. Mengyang Gu acknowledges partial support from the National Science Foundation under Award No. OAC-2411043 and the University of California Multicampus Research Programs and Initiatives under Award No. M23PL599. We thank the editor, associate editor, and three anonymous referees for their comments that substantially improved this article.

Supplementary Material

The Supplementary Material contains (i) proofs of all lemmas; (ii) a summary of the connection between Gaussian processes with Matérn covariance (roughness parameters 0.5 and 2.5) and DLMS,

with closed-form expressions of $\mathbf{F}_{t,j}$, $\mathbf{G}_{t,j}$ and $\mathbf{W}_{t,j}$; (iii) the conjugate gradient algorithm; (iv) procedures for the scalable computation of the predictive distribution in particle dynamics; (v) an application of the IKF-CG algorithm for predicting missing values in lattice data; (vi) parameter estimation methods; (vii) computational complexity analysis; (viii) additional simulation results for estimating particle interaction; and (ix) numerical results for predicting missing values in lattice data.

Appendix A. Kalman Filter

The Kalman filter [17] for dynamic linear models in (1)-(2) is summarized in Lemma A1.

Lemma A1. *Let $\boldsymbol{\theta}_{t-1} \mid \mathbf{y}_{1:t-1} \sim \mathcal{MN}(\mathbf{m}_{t-1}, \mathbf{C}_{t-1})$. Recursively for $t = 2, \dots, N$:*

(i) *The one-step-ahead predictive distribution of $\boldsymbol{\theta}_t$ given $\mathbf{y}_{1:t-1}$ is*

$$\boldsymbol{\theta}_t \mid \mathbf{y}_{1:t-1} \sim \mathcal{MN}(\mathbf{b}_t, \mathbf{B}_t), \quad (26)$$

with $\mathbf{b}_t = \mathbf{G}_t \mathbf{m}_{t-1}$ and $\mathbf{B}_t = \mathbf{G}_t \mathbf{C}_{t-1} \mathbf{G}_t^T + \mathbf{W}_t$.

(ii) *The one-step-ahead predictive distribution of y_t given $\mathbf{y}_{1:t-1}$ is*

$$y_t \mid \mathbf{y}_{1:t-1} \sim \mathcal{N}(f_t, Q_t), \quad (27)$$

with $f_t = \mathbf{F}_t \mathbf{b}_t$, and $Q_t = \mathbf{F}_t \mathbf{B}_t \mathbf{F}_t^T + V_t$.

(iii) *The filtering distribution of $\boldsymbol{\theta}_t$ given $\mathbf{y}_{1:t}$ follows*

$$\boldsymbol{\theta}_t \mid \mathbf{y}_{1:t} \sim \mathcal{MN}(\mathbf{m}_t, \mathbf{C}_t), \quad (28)$$

with $\mathbf{m}_t = \mathbf{b}_t + \mathbf{B}_t \mathbf{F}_t^T Q_t^{-1} (y_t - f_t)$ and $\mathbf{C}_t = \mathbf{B}_t - \mathbf{B}_t \mathbf{F}_t^T Q_t^{-1} \mathbf{F}_t \mathbf{B}_t$.

Lemma A2. *Denote $\tilde{\mathbf{y}} = (\tilde{y}_1, \dots, \tilde{y}_N)^T = \mathbf{L}^{-1} \mathbf{y}$, where \mathbf{L} is the factor in Cholesky decomposition of a positive definite covariance $\boldsymbol{\Sigma}$, with $\boldsymbol{\Sigma} = \text{cov}[\mathbf{y}]$ and $\mathbf{y} = (y_1, \dots, y_N)^T$ defined as in (1). We have*

$$\tilde{y}_t = \frac{y_t - f_t}{Q_t^{\frac{1}{2}}}, \quad (29)$$

where f_t and Q_t are defined in Eq. (27). Furthermore, the t th diagonal term of \mathbf{L} is $L_{t,t} = Q_t^{1/2}$.

References

- [1] Hugues Chaté, Francesco Ginelli, Guillaume Grégoire, Fernando Peruani, and Franck Raynaud. Modeling collective motion: variations on the Vicsek model. *The European Physical Journal B*, 64(3):451–456, 2008.
- [2] Noel Cressie and Gardar Johannesson. Fixed rank kriging for very large spatial data sets. *Journal of the Royal Statistical Society: Series B (Statistical Methodology)*, 70(1):209–226, 2008.
- [3] Abhirup Datta, Sudipto Banerjee, Andrew O Finley, and Alan E Gelfand. Hierarchical nearest-neighbor Gaussian process models for large geostatistical datasets. *Journal of the American Statistical Association*, 111(514):800–812, 2016.

- [4] Daniele Durante and David B Dunson. Nonparametric Bayes dynamic modelling of relational data. *Biometrika*, 101(4):883–898, 2014.
- [5] James Durbin and Siem Jan Koopman. *Time series analysis by state space methods*, volume 38. OUP Oxford, 2012.
- [6] Geir Evensen. *Data assimilation: the ensemble Kalman filter*. Springer Science & Business Media, 2009.
- [7] Andrew O. Finley, Abhirup Datta, and Sudipto Banerjee. spNNGP R Package for Nearest Neighbor Gaussian Process Models. *Journal of Statistical Software*, 103(5):1–40, 2022.
- [8] Reinhard Furrer, Marc G Genton, and Douglas Nychka. Covariance tapering for interpolation of large spatial datasets. *Journal of Computational and Graphical Statistics*, 15(3):502–523, 2006.
- [9] Francesco Ginelli, Fernando Peruani, Markus Bär, and Hugues Chaté. Large-scale collective properties of self-propelled rods. *Physical review letters*, 104(18):184502, 2010.
- [10] Robert B Gramacy and Daniel W Apley. Local Gaussian process approximation for large computer experiments. *Journal of Computational and Graphical Statistics*, 24(2):561–578, 2015.
- [11] Mengyang Gu, Xinyi Fang, and Yizi Lin. *FastGaSP: Fast and Exact Computation of Gaussian Stochastic Process*, 2025. R package version 0.6.1.
- [12] Mengyang Gu, Xiaojing Wang, and James O Berger. Robust Gaussian stochastic process emulation. *Annals of Statistics*, 46(6A):3038–3066, 2018.
- [13] Mark S Handcock and Michael L Stein. A Bayesian analysis of kriging. *Technometrics*, 35(4):403–410, 1993.
- [14] Jouni Hartikainen and Simo Sarkka. Kalman filtering and smoothing solutions to temporal Gaussian process regression models. In *Machine Learning for Signal Processing (MLSP), 2010 IEEE International Workshop on*, pages 379–384. IEEE, 2010.
- [15] Trevor Hastie and Robert Tibshirani. Varying-coefficient models. *Journal of the Royal Statistical Society: Series B (Methodological)*, 55(4):757–779, 1993.
- [16] Magnus R Hestenes and Eduard Stiefel. Methods of conjugate gradients for solving linear systems. *Journal of research of the National Bureau of Standards*, 49(6):409, 1952.
- [17] Rudolph Emil Kalman. A new approach to linear filtering and prediction problems. *Journal of basic Engineering*, 82(1):35–45, 1960.
- [18] Yael Katz, Kolbjørn Tunstrøm, Christos C Ioannou, Cristián Huepe, and Iain D Couzin. Inferring the structure and dynamics of interactions in schooling fish. *Proceedings of the National Academy of Sciences*, 108(46):18720–18725, 2011.
- [19] Matthias Katzfuss and Joseph Guinness. A general framework for Vecchia approximations of Gaussian processes. *Statistical Science*, 36(1):124–141, 2021.

- [20] Matthias Katzfuss, Joseph Guinness, and Earl Lawrence. Scaled Vecchia approximation for fast computer-model emulation. *SIAM/ASA Journal on Uncertainty Quantification*, 10(2):537–554, 2022.
- [21] Genshiro Kitagawa. Monte Carlo filter and smoother for non-Gaussian nonlinear state space models. *Journal of computational and graphical statistics*, 5(1):1–25, 1996.
- [22] Clifford Lam, Qiwei Yao, and Neil Bathia. Estimation of latent factors for high-dimensional time series. *Biometrika*, 98(4):901–918, 2011.
- [23] Finn Lindgren, Håvard Rue, and Johan Lindström. An explicit link between Gaussian fields and Gaussian Markov random fields: the stochastic partial differential equation approach. *Journal of the Royal Statistical Society: Series B (Statistical Methodology)*, 73(4):423–498, 2011.
- [24] Fei Lu, Ming Zhong, Sui Tang, and Mauro Maggioni. Nonparametric inference of interaction laws in systems of agents from trajectory data. *Proceedings of the National Academy of Sciences*, 116(29):14424–14433, 2019.
- [25] Yimin Luo, Mengyang Gu, Minwook Park, Xinyi Fang, Younghoon Kwon, Juan Manuel Urueña, Javier Read de Alaniz, Matthew E Helgeson, Cristina M Marchetti, and Megan T Valentine. Molecular-scale substrate anisotropy, crowding and division drive collective behaviours in cell monolayers. *Journal of the Royal Society Interface*, 20(204):20230160, 2023.
- [26] Suman Majumder, Yawen Guan, Brian J Reich, and Arvind K Saibaba. Kryging: geostatistical analysis of large-scale datasets using Krylov subspace methods. *Statistics and Computing*, 32(5):74, 2022.
- [27] Giovanni Petris, Sonia Petrone, and Patrizia Campagnoli. Dynamic linear models. In *Dynamic linear models with R*. Springer, 2009.
- [28] Raquel Prado and Mike West. *Time series: modeling, computation, and inference*. Chapman and Hall/CRC, 2010.
- [29] Dennis C Rapaport. *The art of molecular dynamics simulation*. Cambridge university press, 2004.
- [30] Arvind K Saibaba, Alen Alexanderian, and Ilse CF Ipsen. Randomized matrix-free trace and log-determinant estimators. *Numerische Mathematik*, 137(2):353–395, 2017.
- [31] Edward Snelson and Zoubin Ghahramani. Sparse Gaussian processes using pseudo-inputs. *Advances in neural information processing systems*, 18:1257, 2006.
- [32] Michael L Stein. *Interpolation of spatial data: some theory for kriging*. Springer Science & Business Media, 2012.
- [33] Michael L Stein, Jie Chen, and Mihai Anitescu. Stochastic approximation of score functions for Gaussian processes. *The Annals of Applied Statistics*, 7(2):1162–1191, 2013.
- [34] Jonathan R Stroud, Michael L Stein, Barry M Lesht, David J Schwab, and Dmitry Beletsky. An ensemble Kalman filter and smoother for satellite data assimilation. *Journal of the american statistical association*, 105(491):978–990, 2010.

- [35] Aldo V Vecchia. Estimation and model identification for continuous spatial processes. *Journal of the Royal Statistical Society: Series B (Methodological)*, 50(2):297–312, 1988.
- [36] Tamás Vicsek, András Czirók, Eshel Ben-Jacob, Inon Cohen, and Ofer Shochet. Novel type of phase transition in a system of self-driven particles. *Physical review letters*, 75(6):1226, 1995.
- [37] Elise Walck-Shannon and Jeff Hardin. Cell intercalation from top to bottom. *Nature Reviews Molecular Cell Biology*, 15(1):34–48, 2014.
- [38] M. West and P. J. Harrison. *Bayesian Forecasting & Dynamic Models*. Springer Verlag, 2nd edition, 1997.
- [39] Peter Whittle. On stationary processes in the plane. *Biometrika*, pages 434–449, 1954.